Shape Control of Bimetallic MOF/Graphene Composites for Efficient Oxygen Evolution Reaction

Zhi Li, *[a,c] Yiming Guo, [b] Kai Li, [a,c] Shuang Wang, [a,c] Enrico De Bonis, [d] Hai Cao, [b] Stijn F. L. Mertens,* [d] Chao Teng *[c]

a. National Laboratory of Solid State Microstructures, College of Engineering and Applied Sciences, Nanjing University, Nanjing 210093, China.

b. State Key Laboratory of Materials-Oriented Chemical Engineering, College of Chemical Engineering, Nanjing Tech University, Nanjing 211816, China.

c. Institute of Marine Biomedicine, Shenzhen Polytechnic, Shenzhen 518055, China.

d. Department of Chemistry, Energy Lancaster and Materials Science Institute, Lancaster University, Bailrigg, Lancaster LA1 4YB, United Kingdom

*Corresponding authors. lizhireal@163.com (Z. Li); s.mertens@lancaster.ac.uk (S.F.L. Mertens); tengchao@szpt.edu.cn (C. Teng)

Highly efficient and stable earth-abundant metal electrocatalysts are of great significance for improving water splitting systems and rechargeable metal–air batteries, in which the oxygen evolution reaction (OER) plays a central part. Among other strategies, anchoring metal-organic frameworks (MOFs) onto conductive materials has proven fruitful towards enhancing their OER performance. Here we explore two strategies for covalent functionalization of graphene flakes as templates for *in situ* growth of a bimetallic MOF (NiCo-H_2bpydc) that is formed using 2,2'-bipyridine-5,5'-dicarboxylic acid as the organic linker, and Ni^{2+}/ Co^{2+} (1:1) as the metal nodes. The graphene template modified with low density functional groups preserves the original octahedral shape of 3D NiCo-H_2bpydc, while functionalization with high density functional groups transforms the MOF octahedra into nanoflowers with 'desert rose' morphology, leading to increased accessible active sites, electric conductivity and enlarged active surface area, thus boosting the OER performance with a small overpotential (241mV) at 10 mA cm^{-2} in alkaline solution. This synthetic strategy therefore presents an efficient pathway towards controlling morphology and properties of graphene supported electrocatalytic materials with excellent OER performance.

Keywords: oxygen evolution reaction, covalent functionalization, graphene template, bimetallic, metal organic framework

1. Introduction

As society transitions from fossil fuels to renewable energy sources, substantial efforts are invested in improving technologies such as water splitting systems and rechargeable metal-air batteries, in which the oxygen evolution reaction (OER) plays a central role [1-3]. However, the sluggish

reaction kinetics and large overpotential make the OER a major bottleneck [4-6]. While noble metal oxides such as IrO_2 and RuO_2 are still among the most efficient OER catalysts, their scarcity and high cost severely restrict their industrial scale application. The discovery of high-efficiency, low-cost, and durable catalysts for OER is therefore of great significance and expected to have immense economic, environmental, and societal impact [7]. In this context, much work has been devoted to the study of metal–organic frameworks (MOFs), whose structural and chemical versatility (through choice of ligands and metal nodes) gives access to a vast variety of materials [8-11]. Considerable challenges still exist, however, as bulk MOFs often suffer from low electric conductivity and mass permeability, which have a direct negative impact on electrocatalytic activity.

In order to solve these problems, the use of ultrathin 2D MOF nanosheets holds substantial promise due to their high specific surface area, significantly enhanced presence of unsaturated active sites (dangling bonds) and faster electron and mass transfer rates [12-16]. Furthermore, synergistic effects in bimetallic MOFs allow tailoring the electronic structure of the metal active sites and enhancing their catalytic activity [17-22]. Combining catalysts with highly conductive carbon materials such as graphene, graphene oxide (GO) and carbon nanotubes (CNTs) improve electric conductivity and specific surface area [23-25], again enhancing catalytic performance. However, simple mechanical blending of the conducting materials with 2D MOFs only gives marginal improvement of OER performance due to inefficient electronic communication between the MOFs and the conductive substrates. Covalent anchoring of MOFs on conducting materials on the other hand, by efficiently producing overlapping electron clouds, leads to large improvements in electrocatalytic activity [26]. We recently exploited the same concept in covalently linking β-cyclodextrin to graphite for constructing an electrochemical sensor with high selectivity for hydrophobic analytes, producing the highest sensitivity for dopamine to date for a cyclodextrin-based sensor [27].

In this work, we synthesized an octahedral, bimetallic MOF (NiCo-H_2bpydc) with Ni^{2+} and Co^{2+} as the metal nodes and 2,2'-bipyridine-5,5'-dicarboxylic acid (H_2bpydc) molecules as organic linkers. Besides synthesising and characterising this MOF benchmark material, we explore to what extent covalent modification of graphene flakes allows shape control

during *in situ* MOF growth, forming MOF/graphene composites. To this end, graphene flakes were covalently modified with 4-aminobenzoic acid (G-COOH) and 1-aminobenzene-3,4,5-tricarboxylic acid (G-3COOH), and used as templates for directing the growth of NiCo-H2bpydc. We found that the NiCo-H_2bpydc grows on the G-COOH substrate without changing its original structure (NiCo-H_2bpydc@G-COOH), while the G-3COOH substrate transforms the octahedra into slit-like nanoflowers (NiCo-H_2bpydc@G-3COOH), enlarging the specific surface area, increasing the accessible unsaturated active sites, and boosting the OER performance.

2. Experimental

2.1. Chemicals

2,2'-Bipyridine-5,5'-dicarboxylic acid (H_2bpydc) was bought from Hao Hong Pharma with a purity of 98%. The graphene nanosheet was bought from XFNANO Materials Tech 1-5 nm in thickness and 5.0 μm in lateral size. Sodium nitrite ($NaNO_2$, 99.99%), iridium(IV) oxide (IrO_2, 99.9%), nickel(II) acetate (99.9%), cobalt(II) acetate (99.9%), and hypophosphorous acid (HPO3, 50%) were purchased from Macklin. N,N-dimethylformamide (DMF, 99.5%) and 4-aminobenzoic acid (99.5%) were purchased from Sinopharm, reagent grade hydrochloric acid from YongHua Chemical, Nafion solution (5%) and potassium hydroxide (KOH, 99.99%) from Alfa Aesar, 1-aminobenzene-3,4,5-tricarboxylic acid (96%), acetonitrile (98%) and methanol (analytical grade) from Aladdin.

2.2. Synthetic procedures

NiCo-H_2bpydc MOF was synthesised by preparing 0.5 mM nickel(II) acetate, 0.5 mM cobalt acetate and 1mM 2,2'-bipyridine-5,5'-dicarboxylic acid in 14 ml DMF + 1ml H_2O. After stirring for 30 mins, the resulting mixture was transferred to a 20 ml PTFE-lined stainless steel container, heated to 393 K for 48 hours in a programmed oven and cooled to room temperature. The grey solid product was obtained via centrifugation and washed with DMF and anhydrous methanol several times, followed by drying in a vacuum oven at 333K overnight. G-COOH and G-3COOH were prepared by covalent modification of graphene flakes with 4-aminobenzoic acid or 1-aminobenzene-3,4,5-tricarboxylic acid via chemically activated one-electron reduction of the corresponding diazonium compound using

HPO_3 (50% aqueous solution) according to the previously reported method [28]. The starting graphene flakes were sonicated for 1 h in water prior to use. Taking the preparation of G-COOH as an example, a 20 mM solution of 4-aminobenzoic acid was prepared in 0.1M HCl at 298K (10 ml), and then the equivalent amount of $NaNO_2$ was added under stirring. After mixing the resulting 4-carboxylbenzene diazonium with graphene flakes (50 mg), the mixture was stirred at 298K. Afterwards, 20 ml HPO_3 was slowly added and the mixture was stirred for 2 h. The resulting 4-aminobenzoic acid modified graphene (G-COOH) was then filtered and washed with copious quantities of acetonitrile, methanol and water to remove any unreacted, physisorbed species, followed by overnight drying in a vacuum oven at 333K. G-3COOH was prepared following the same procedure, using 1-aminobenzene-3,4,5-tricarboxylic acid instead of 4-aminobenzoic acid. NiCo-H_2bpydc@G-COOH was prepared as follows. G-COOH was sonicated in 14 mL DMF and 1ml H_2O for 30 min before use. Afterwards, 0.5 mM nickel(II) acetate and 0.5 mM cobalt acetate were dissolved in the G-COOH dispersion under stirring, followed by adding 1mM 2,2'-bipyridine-5,5'-dicarboxylic acid and stirring for 30 min. The mixture was transferred to a 20 ml Teflon-lined stainless steel container, heated to 393 K for 48 hours in a programmed oven and cooled to room temperature. The grey solid product was obtained via centrifugation and washed with DMF and anhydrous methanol several times, followed by drying in a vacuum oven at 333K overnight. NiCo-H_2bpydc@G-3COOH was prepared following the same procedure but using G-3COOH instead of G-COOH.

2.3 Characterisation

Field emission-scanning electron microscope (FE-SEM) images and energy dispersive spectroscopy (EDS) were recorded in a Regulus 8220 and S-4800 instrument. X-ray diffraction (XRD) spectra were measured on a Smartlab TM 9KW (Cu Kα1). Raman spectra were obtained using a LabRAM HR spectrometer. The nitrogen adsorption-desorption isotherms were performed at 77 K using an ASAP2020M system. The X-ray photoelectron spectra (XPS) was measured on an AXIS SUPRA spectrometer.

2.4 Electrochemical measurements

The electrochemical measurements were conducted using a Corrtest CS300H electrochemical workstation. All the measurements were carried out in 1M KOH solution using a three-electrode configuration, and all potentials measured were converted to the reversible hydrogen electrode (RHE) scale through the following equation: $E_{RHE} = E + 0.197\ V + 0.0592\ pH$. The working electrode was prepared by uniformly coating 5 μL catalyst ink (using ethanol/water 1:1 as dispersing agent) on a glassy carbon rotating disc electrode (3 mm diameter). The solvent was allowed to evaporate naturally without heating, which took several hours. A mass loading of 0.36 mg cm^{-2} was used, and the rotation speed was set to 800 rpm to ensure well-behaved mass transport and remove any bubbles from the electrode surface. A silver/silver chloride (Ag/AgCl/saturated KCl) was used as the reference electrode (RE), and platinum foil (1 cm × 1 cm) as the counter electrode (CE). Cyclic voltammograms (CV) were obtained in the capacitive potential region using a scan rate of 50 mV s^{-1}. Linear sweep voltammetry (LSV) was performed at a scan rate of 5 mV s^{-1} to minimise capacitive current. Tafel slopes were obtained from their corresponding polarisation curves. Long-term electrode stability was evaluated through potentiostatic measurement at an overpotential of 250 mV at a rotation rate of 800 rpm for 50000 s (= 13.9 h). Electrochemical impedance spectra (EIS) were recorded at the open-circuit potential over the frequency range from 10^5 Hz to 0.01 Hz, using an excitation sine wave with an amplitude of 10 mV rms.

3. Results and discussion

Direct solvothermal synthesis of pristine NiCo-H_2bpydc was achieved by reacting H_2bpydc with Ni^{2+} and Co^{2+} in N,N'-dimethylformamide (DMF) at 120 ℃for 48 h, as illustrated in **Figure 1**a. The preparation of graphene supported NiCo-H_2bpydc is shown in Figure 1b. Following pathway 1, the NiCo-H_2bpydc@G-COOH composite was synthesized by incorporating G-COOH as the template to support the growth of 3D NiCo-H_2bpydc MOF. The G-COOH template was prepared by covalent modification of graphene flakes with 4-aminobenzoic acid. Because the 3- and 5-positions of the pre-grafted aryl molecules are subjected to the attack of subsequent aryl radicals, covalent functionalization of graphene by aryldiazonium molecules with a functional group in the 4-position tends to form a low-density multilayer dendrite-like structure [29, 30]. Following pathway 2, NiCo-H_2bpydc@G-3COOH was prepared by incorporating G-3COOH as the template to

support the growth of NiCo-H_2bpydc nanoflowers that contain slit-like arrays. The G-3COOH template was formed by covalent functionalization of graphene flakes with 1-aminobenzene-3,4,5-tricarboxylic acid. In this case, the 3,4,5-positions are blocked by carboxylic groups, which hinder the further attack on the pre-grafted molecules and lead to high-density monolayer functionalization [30].

The morphologies of the pristine graphene flakes, NiCo-H_2bpydc MOFs, NiCo-H_2bpydc@G-COOH and NiCo-H_2bpydc@G-3COOH were investigated using SEM, **Figure 2**. Figure 2a shows pristine graphene flakes, whose size is in the range of a few μm. The corresponding EDS analysis shows mainly carbon (~97.75%) and oxygen as a minor component (~2.25%, Figure S1). Octahedral structures can be clearly recognised in Figure 2b, confirming the successful formation of 3D networks of pristine NiCo-H_2bpydc MOF, similar to the morphology reported for Zr(IV)-UiO-67-BPY containing Zr^{4+} metal nodes and H_2bpydc ligands [31-33]. The inset of Figure 2b shows a high-resolution SEM image of a NiCo-H_2bpydc MOF octahedron with 4-5 μm size, while EDS analysis shows the presence of Ni, Co, C, O and N, indicating that the product contains both metals (Ni and Co) and the H_2bpydc ligand, Figure S1. When G-COOH is used for directing the formation of NiCo-H_2bpydc@G-COOH, the octahedral shape of the bimetallic MOF is preserved, Figure 2c, though somewhat smaller octahedra of 2-3 μm are obtained. Similar observations were made in previous work, in which the shape of the rhombic dodecahedral ZnCo-zeolite imidazole framework (ZIF) was preserved during graphene oxide-directed *in situ* growth [21].

By contrast, the use of G-3COOH as a template for MOF growth leads to a very different morphology consisting of clusters of nanoflowers, Figure 2d. The striking morphology is reminiscent of 'desert rose' crystals that are formed in arid environments through slow evaporation of water-soluble minerals such as gypsum and baryte [34], and that are characterised by pronounced flattening along the c-axis. A full elucidation of the mechanism of formation of NiCo-H_2bpydc@G-3COOH is beyond the scope of this paper, but it is likely that the large number of carboxylic acid groups on the G-3COOH template changes the nucleation and growth balance sufficiently to steer the product shape. It is expected that the surface area and the number of exposed active sites on this material are very different from the

octahedral crystals. We also anticipate this morphology may have significant impact on electrochemical characteristics, as these are intimately linked to interfacial properties. Similar effects were previously demonstrated during fast charging and discharging of desert rose shaped $LiCoO_2$ [35].

The chemical composition and structural characterisation of NiCo-H_2bpydc@G-3COOH are shown in **Figure 3**. The X-ray photoelectron spectroscopy (XPS) survey confirms the co-existence of Ni, Co, C, O and N in the NiCo-H_2bpydc@G-3COOH and finds no evidence for other impurities (Figure 3a). High-resolution XPS scans for C_{1s} of NiCo-H_2bpydc@G-3COOH and graphene are shown in Figure 3b. The presence of the distinct O-C=O peak indicates the existence of a large number of –COOH groups in NiCo-H_2bpydc@G-3COOH and a significant enhancement for the peak area ratio of C-C sp^3 / C-C sp^2 was observed in NiCo-H_2bpydc@G-3COOH, which is caused by the high-density anchoring of 1-aminobenzene-3,4,5-tricarboxylic acid molecules on graphene through covalent grafting. Further details of the graphene surface state can be directly probed by Raman spectroscopy [36, 37]. In particular, the intensity of the d peak in the Raman spectra of graphene-based samples is strongly related to lattice defects, including those caused by the formation of sp^3 carbons following covalent functionalization. While many other effects factor into the d peak intensity, there is a consensus that the intensity ratio between d and g peaks (I_d/I_g) can be used to roughly evaluate the degree of covalent functionalization of graphene and graphitic surfaces [38]. Figure 3c shows that the pristine graphene flakes have low defect density, as the ratio I_d/I_g equals 0.13. After low-density covalent modification with 4-aminobenzoic acid, this ratio triples (I_d/I_g = 0.39), while the d and g peaks reach almost equal intensity (I_d/I_g = 0.91) in high-density grafted G-3COOH. The crystal structure of graphene flakes, pristine NiCo-H_2bpydc, G-COOH and G-3COOH templated NiCo-H_2bpydc was characterized by XRD, Figure 3d. The bimetallic 3D NiCo-H_2bpydc MOF shows a similar XRD pattern to the previously reported UiO-67–BPY with peaks at 5.76° (1 1 1), 6.66° (2 0 0) and 9.46° (2 2 0), respectively [31-33]. The XRD pattern of G-COOH directed NiCo-H_2bpydc@G-COOH is similar to the pristine MOF, confirming that in addition to the octahedral morphology (Figure 2), also the crystal structure is maintained when growing NiCo-H_2bpydc on the G-COOH template. However, the G-3COOH substrate directed growth of

NiCo-H_2bpydc shows a fundamentally different XRD pattern, indicating that the original crystal structure of NiCo-H_2bpydc is transformed, and that a new crystallographic phase is present. By ignoring the graphene reflection, the remaining reflections can be indexed to a primitive unit cell measuring: 6.97 (Å), 6.97, 23.8, 90 (deg), 90, 90, 1158.8 (Å^3), using EXPO2014 [39]. A full structural elucidation of the desert rose phase is, however, outside the scope of this paper, and may be hindered by the fact that the desert rose phase has one very thin dimension that is unlikely to generate clear XRD reflections, so that an apparent high-symmetry phase could be select reflections from a low-symmetry one.

The electrocatalytic OER performance of as-prepared NiCo-H_2bpydc, NiCo-H_2bpydc@G-COOH and NiCo-H_2bpydc@G-3COOH was evaluated after deposition on a glassy carbon electrode with a mass loading of 0.36 mg cm^{-2} and measuring in 1M KOH, using a conventional three-electrode system, **Figure 4**. For comparison, also mechanically blended graphene flakes with NiCo-H_2bpydc (G/NiCo-H_2bpydc) and commercial IrO_2 are evaluated. In the polarization curves, the oxidations peaks in the potential regions from 1.17 V to 1.45V can be attributed to the oxidation of Ni cations [12]. As shown in **Figure 4a**, the NiCo-H_2bpydc@G-3COOH exhibits a significantly higher current density for electrocatalytic OER, with the lowest overpotential (The E_0 H_2O/O_2 = 1.229 V as reference) of 241 mV to reach 10 mA cm^{-2}, compared to NiCo-H_2bpydc (E_{10} = 431 mV), NiCo-H_2bpydc@G-COOH (E_{10} = 279 mV), G/NiCo-H_2bpydc (E_{10} = 384 mV) and commercial IrO_2 (E_{10} = 319 mV). In addition, the OER performance of NiCo-H_2bpydc@G-3COOH is better than the most of the NiCo based catalysts reported to date under similar conditions (Table S1). Tafel analysis, **Figure 4b**, produces the lowest Tafel slope for NiCo-H_2bpydc@G-3COOH (95 mV dec^{-1}), compared to NiCo-H_2bpydc@G-COOH (146 mV dec^{-1}), NiCo-H_2bpydc (137 mV dec^{-1}) and G/NiCo-H_2bpydc (114 mV dec^{-1}), indicating the most favourable OER kinetics are observed for NiCo-H_2bpydc@G-3COOH.

In order to analyse in greater detail the origin of the variation in electrocatalytic activity, and also quantify the effect of extensive covalent functionalisation of the graphene template, we carried out impedance measurements in the electrolyte used for OER, **Figure 5**. While the Nyquist plots suggest a single semicircle—a consequence of the linear scale, and the

compression of more than half of the spectrum in one corner of the graph [40-41]—Bode plots clearly show the presence of at least two time constants. The equivalent circuit shown is the simplest that provides a good quality fit; apart from the uncompensated electrolyte resistance R1 we attribute the two RQ combinations with the behaviour of the electrode–catalyst interface and with the catalyst–electrolyte interface; the parameter values for the 4 different electrode materials are summarised in Table S2. Focussing for now on the resistive elements, the values of R2 are in the low ohm range for all 4 electrodes, suggesting that even introduction of large numbers of sp^3 defects in the graphene template (as is the case for NiCo-H_2bpydc@G-3COOH) is not detrimental to the material's conductivity. Crucial for the electrocatalytic properties, the charge transfer resistance R2 of the 3 MOF materials lines up in the same order in which the OER overpotential increases, confirming that these effects are mechanistic in nature and not related to resistive losses.

The better performance can be attributed to the higher electron transfer efficiency generated by the introduction of graphene and the more exposed unsaturated active sites via the transformation of octahedral structure to arrays. The increased surface area may also contribute to the enhancement of OER performance. The Brunauer-Emmett-Teller (BET) surface area (Figure S3) of NiCo-H_2bpydc@G-3COOH (128.7 m^2 g^{-1}) is almost twice the value of NiCo-H_2bpydc (71.8 m^2 g^{-1}). In addition, the N_2 adsorption-desorption isotherm of NiCo-H_2bpydc@G-3COOH shows a typical type II isotherm with H4-type hysteresis loop, in agreement with the formation of a mesoporous structure (i.e., the desert rose phase) via the aggregation of the arrays anchored on graphene flakes [26, 42].

As the double layer behaviour based on impedance measurements can be complicated by constant phase element behaviour, we extracted electrochemically active surface area from the double-layer capacitance (C_{dl}) in cyclic voltammograms where no faradaic processes take place, Figure S3. The is employed to evaluate the electrochemically active surface area. As shown in Figure S4, the C_{dl} of NiCo-H_2bpydc@G-3COOH (1.80 mF cm^{-2}) is ten times higher than that of NiCo-H_2bpydc (0.17 mF cm^{-2}), a factor five higher than the increase of physical surface area based on gas adsorption discussed above.

In view of the profound effect of the graphene template on the resulting MOF morphology in the case of G-3COOH and on the OER characteristics, the G-3COOH/MOF mass ratio on the OER performance was also evaluated, **Figure 4c**. We observe that the overpotential for OER decreases as the G-3COOH/MOF mass ratio increases from 4% (E_{10}=295 mV) to 6% (E_{10}=280 mV), reaches a minimum at 8% (E_{10}=241 mV), and increases again beyond this point (E_{10}=270 mV for G-3COOH/MOF = 10%). In line with previous work on bimetallic MOFs [17-22], **Figure 4d** confirms the synergistic effect of the two metals in NiCo-H_2bpydc@G-3COOH. Compared to NiCo-H_2bpydc@G-3COOH, higher overpotentials for electrocatalytic OER are generated by either of the corresponding single-metal materials Ni-H_2bpydc@G-3COOH (E_{10}=293 mV) and Co-H_2bpydc@G-3COOH (E_{10}=352 mV) under otherwise identical circumstances. In a recent operando X-ray absorption study, the optimal electrocatalytic activity at a 50/50 atomic Ni/Co ratio was ascribed to the formation of a reactive $Ni_{0.5}Co_{0.5}OOH_{0.75}$ species at the potentials where high OER activity is observed [22]. We hypothesise that for the desert rose NiCo-H_2bpydc@G-3COOH phase, the formation of this species under reaction conditions is particularly effective.

In addition to the electrocatalytic activity itself, the stability of any electrocatalyst under reaction conditions is vital for any applications. As shown in **Figure 5**, the NiCo-H_2bpydc@G-3COOH retains 94.5% of its initial activity after 50000 s (~13.9 h) of continuous OER at an overpotential of 250 mV, while often cited IrO_2 retains only 62.8%, indicating excellent long-term stability of the NiCo 'desert rose' electrocatalyst. SEM imaging after the long-term test, **Figure S5**, reveals virtually unchanged desert rose morphology of NiCo-H_2bpydc@G-3COOH, despite the structural changes under operando conditions [22].

4. Conclusions

In this paper, we have explored two different functionalization strategies for anchoring graphene with low and high density of functional groups for the *in situ* growth of MOFs. The two graphene templates are helpful for the improvement of the OER performance of in situ grown MOFs. The G-COOH template with low density of functional groups retains the original octahedral morphology of NiCo-H_2bpydc, while the G-3COOH template

with high density of functional groups transforms the MOF octahedra into ‘desert rose’ shaped nanoflowers, increasing the active sites and enlarging the surface area, and overall boosting OER performance in alkaline solution. Our results show that covalent modification of graphene can profoundly change structure, morphology and electrocatalytic properties of materials that are subsequently grown on these templates, for instance using solvothermal methods.

Credit author statement

Zhi Li: Conceptualization, Methodology, Validation, Formal analysis, Investigation, Visualization, Writing-Original Draft; Yiming Guo: Investigation, Visualization; Kai Li and Shuang Wang: Discussion, Editing; Enrico De Bonis: Formal analysis, Visualisation; Stijn F. L. Mertens: Formal analysis, Writing-Review & Editing; Hai Cao: Supervision, Funding acquisition, Writing-Review & Editing; Chao Teng: Supervision, Funding acquisition, Writing-Review & Editing, Project administration.

Conflicts of interest

There are no conflicts to declare.

Acknowledgements

This research was funded by Science &Technology Department of Jiangsu Province, Nanjing Tech University and State Key Laboratory of Materials-Oriented Chemical Engineering, Shenzhen Science and Technology Innovation Commission (GJHZ20190819151807167 and JSGG20200103094001790) and Post-doctoral Foundation Project of Shenzhen Polytechnic (grant no. 6020330009K, grant no. 6020330008K, grant no.6021330004K). EDB and SFLM acknowledge internal funds from Materials Science Lancaster and thank Dr Nathan Halcovitch for help with XRD analysis.

[1] Z. Xue, Y. Li, Y. Zhang, W. Geng, B. Jia, J. Tang, S. Bao, H.P. Wang, Y. Fan, Z.w. Wei, Modulating electronic structure of metal−organic framework for efficient electrocatalytic oxygen evolution, Advanced Energy Materials, 8 (2018) 1801564. doi: 10.1002/aenm.201801564

[2] X.L. Wang, L.Z. Dong, M. Qiao, Y.J. Tang, J. Liu, Y. Li, S.L. Li, J.X. Su, Y.Q. Lan, Exploring the performance improvement of the oxygen evolution reaction in a stable

bimetal–organic framework system, Angewandte Chemie International Edition, 57 (2018) 9660-9664. doi: 10.1002/anie.201803587
[3] Z. Li, H. He, H. Cao, S. Sun, W. Diao, D. Gao, P. Lu, S. Zhang, Z. Guo, M. Li, Atomic Co/Ni dual sites and Co/Ni alloy nanoparticles in N-doped porous Janus-like carbon frameworks for bifunctional oxygen electrocatalysis, Applied Catalysis B: Environmental, 240 (2019) 112-121. doi: 10.1016/j.apcatb.2018.08.074
[4] S. Farid, S. Ren, C. Hao, MOF-derived metal/carbon materials as oxygen evolution reaction catalysts, Inorganic Chemistry Communications, 94 (2018) 57-74. doi: 10.1016/j.inoche.2018.06.008
[5] C. Guo, Y. Zheng, J. Ran, F. Xie, M. Jaroniec, S.Z. Qiao, Engineering high‐energy interfacial structures for high−performance oxygen−involving electrocatalysis, Angewandte Chemie International Edition, 56 (2017) 8539-8543. doi: 10.1002/anie.201701531
[6] X. Jia, Y. Zhao, G. Chen, L. Shang, R. Shi, X. Kang, G.I. Waterhouse, L.Z. Wu, C.H. Tung, T. Zhang, Ni_3FeN nanoparticles derived from ultrathin NiFe−layered double hydroxide nanosheets: an efficient overall water splitting electrocatalyst, Advanced Energy Materials, 6 (2016) 1502585. doi: 10.1002/aenm.201502585
[7] M. Müllner, M. Riva, F. Kraushofer, M.Schmid, G. S. Parkinson, S. F. L. Mertens, U. Diebold, Stability and catalytic performance of reconstructed Fe_3O_4(001) and Fe_3O_4(110) surfaces during oxygen evolution reaction, Journal of Physical Chemistry C, 123 (2019) 8304–8311. doi: 10.1021/acs.jpcc.8b08733
[8] X. Zhang, J. Luo, K. Wan, D. Plessers, B. Sels, J. Song, L. Chen, T. Zhang, P. Tang, J.R. Morante, From rational design of a new bimetallic MOF family with tunable linkers to OER catalysts, Journal of materials chemistry A, 7 (2019) 1616-1628. doi: 10.1039/C8TA08508K
[9] L. Tao, C.-Y. Lin, S. Dou, S. Feng, D. Chen, D. Liu, J. Huo, Z. Xia, S. Wang, Creating coordinatively unsaturated metal sites in metal-organic-frameworks as efficient electrocatalysts for the oxygen evolution reaction: Insights into the active centers, Nano Energy, 41 (2017) 417-425. doi: 10.1016/j.nanoen.2017.09.055
[10] L. Jiao, Y. Wang, H.L. Jiang, Q. Xu, Metal–organic frameworks as platforms for catalytic applications, Advanced Materials, 30 (2018) 1703663. doi: 10.1002/adma.201703663
[11] B. Li, H. M. Wen, Y. Cui, W. Zhou, G. Qian, B. Chen, Emerging multifunctional metal–organic framework materials, Advanced Materials, 28 (2016) 8819-8860. doi: 10.1002/adma.201601133
[12] S. Zhao, Y. Wang, J. Dong, C.-T. He, H. Yin, P. An, K. Zhao, X. Zhang, C. Gao, L. Zhang, J. Lu, J. Wang, J. Zhang, A. M. Khattak, N. A. Khan, Z. Wei, J. Zhang, S. Liu, H. Zhao, Z. Tang, Ultrathin metal–organic framework nanosheets for electrocatalytic oxygen evolution, Nature Energy, 1 (2016) 1-10. doi: 10.1038/nenergy.2016.184
[13] W. Li, W. Fang, C. Wu, K.N. Dinh, H. Ren, L. Zhao, C. Liu, Q. Yan, Bimetal–MOF nanosheets as efficient bifunctional electrocatalysts for oxygen evolution and nitrogen reduction reaction, Journal of Materials Chemistry A, 8 (2020) 3658-3666. doi: 10.1039/C9TA13473E
[14] D. Zhu, M. Qiao, J. Liu, T. Tao, C. Guo, Engineering pristine 2D metal–organic framework nanosheets for electrocatalysis, Journal of Materials Chemistry A, 8 (2020) 8143-8170. doi: 10.1039/D0TA03138K

[15] T. Kambe, R. Sakamoto, K. Hoshiko, K. Takada, M. Miyachi, J.-H. Ryu, S. Sasaki, J. Kim, K. Nakazato, M. Takata, π-Conjugated nickel bis (dithiolene) complex nanosheet, Journal of the American Chemical Society, 135 (2013) 2462-2465. doi: 10.1021/ja312380b
[16] D. Zhu, C. Guo, J. Liu, L. Wang, Y. Du, S.-Z. Qiao, Two-dimensional metal–organic frameworks with high oxidation states for efficient electrocatalytic urea oxidation, Chemical communications, 53 (2017) 10906-10909. doi: 10.1039/C7CC06378D
[17] Y. Wang, L. Huang, L. Ai, M. Wang, Z. Fan, J. Jiang, H. Sun, S. Wang, Ultrathin nickel-cobalt inorganic-organic hydroxide hybrid nanobelts as highly efficient electrocatalysts for oxygen evolution reaction, Electrochimica Acta, 318 (2019) 966-976. doi: 10.1016/j.electacta.2019.06.079
[18] S. Zhu, A. Xie, X. Tao, J. Zhang, B. Wei, Z. Liu, Y. Tao, S. Luo, Enhanced electrocatalytic performance of CoCu-MOF/polyaniline for glycerol oxidation, Journal of Electroanalytical Chemistry, 857 (2020) 113748. doi: 10.1016/j.jelechem.2019.113748
[19] J. Sun, H. Yin, P. Liu, Y. Wang, X. Yao, Z. Tang, H. Zhao, Molecular engineering of Ni–/Co–porphyrin multilayers on reduced graphene oxide sheets as bifunctional catalysts for oxygen evolution and oxygen reduction reactions, Chemical science, 7 (2016) 5640-5646. doi: 10.1039/C6SC02083F
[20] D.S. Raja, H.-W. Lin, S.-Y. Lu, Synergistically well-mixed MOFs grown on nickel foam as highly efficient durable bifunctional electrocatalysts for overall water splitting at high current densities, Nano Energy, 57 (2019) 1-13. doi: 10.1016/j.nanoen.2018.12.018
[21] Y. Xiao, B. Guo, J. Zhang, C. Hu, R. Ma, D. Wang, J. Wang, A bimetallic MOF@ graphene oxide composite as an efficient bifunctional oxygen electrocatalyst for rechargeable Zn–air batteries, Dalton Transactions, 49 (2020) 5730-5735. doi: 10.1039/D0DT00976H
[22] S. Zhao, C. Tan, C.-T. He, P. An, F. Xie, S. Jiang, Y. Zhu, K.-H. Wu, B. Zhang, H. Li, Structural transformation of highly active metal–organic framework electrocatalysts during the oxygen evolution reaction, Nature Energy, 5 (2020) 881-890. doi: 10.1038/s41560-020-00709-1
[23] M. Wang, M. Lin, J. Li, L. Huang, Z. Zhuang, C. Lin, L. Zhou, L. Mai, Metal–organic framework derived carbon-confined Ni_2P nanocrystals supported on graphene for an efficient oxygen evolution reaction, Chemical Communications, 53 (2017) 8372-8375. doi: 10.1039/C7CC03558F
[24] S. Xue, W. Zhang, Q. Zhang, J. Du, H.-M. Cheng, W. Ren, Heterostructured Ni–Mo–N nanoparticles decorated on reduced graphene oxide as efficient and robust electrocatalyst for hydrogen evolution reaction, Carbon, 165 (2020) 122-128. doi: 10.1016/j.carbon.2020.04.066
[25] A. Majeed, X. Li, P.-X. Hou, H. Tabassum, L. Zhang, C. Liu, H.-M. Cheng, Monolayer carbon-encapsulated Mo-doped Ni nanoparticles anchored on single-wall carbon nanotube film for total water splitting, Applied Catalysis B: Environmental, 269 (2020) 118823. doi: 10.1016/j.apcatb.2020.118823
[26] G. Hai, Z. Tao, H. Gao, J. Zhao, D. Jia, X. Huang, X. Chen, X. Xue, S. Feng, G. Wang, Targeted synthesis of covalently linked Ni-MOFs nanosheets/graphene for oxygen evolution reaction by computational screening of anchoring primers, Nano Energy, 79 (2021) 105418. doi: 10.1016/j.nanoen.2020.105418

[27] Z. Li, J. F. R. Van Guyse, V. R. de la Rosa, H. Van Gorp, P. Walke, H. Uji-i, R. Hoogenboom, S. De Feyter, S. F. L. Mertens, One-step covalent immobilization of β-cyclodextrin on sp^2 carbon surfaces for selective trace amount probing of guests. Advanced Functional Materials, 29(2019) 1901488. doi: 10.1002/adfm.201901488
[28] A.T. Masheter, G.G. Wildgoose, A. Crossley, J.H. Jones, R.G. Compton, A facile method of modifying graphite powder with aminophenyl groups in bulk quantities, Journal of Materials Chemistry, 17 (2007) 3008-3014. doi: 10.1039/B704118G
[29] J. Greenwood, T.H. Phan, Y. Fujita, Z. Li, O. Ivasenko, W. Vanderlinden, H. Van Gorp, W. Frederickx, G. Lu, K. Tahara, Covalent modification of graphene and graphite using diazonium chemistry: Tunable grafting and nanomanipulation, ACS Nano, 9 (2015) 5520-5535. doi: 10.1021/acsnano.5b01580
[30] K. Tahara, Y. Kubo, B. Lindner, S. Hashimoto, S. Hirose, A. Brown, B. Hirsch, L. Daukiya, S. De Feyter, Y. Tobe, Steric and electronic effects of electrochemically generated aryl radicals on grafting of the graphite surface, Langmuir, 35 (2019) 2089-2098. doi: 10.1021/acs.langmuir.8b03339
[31] H. Fei, S.M. Cohen, A robust, catalytic metal–organic framework with open 2, 2′-bipyridine sites, Chemical Communications, 50 (2014) 4810-4812. doi: 10.1039/C4CC01607F
[32] S.-H. Wu, S. Wang, W.-L. Fang, X.-F. Guo, H. Wang, An exceptionally stable Zr-based fluorescent metal–organic framework for highly selective detection of pH, Analytical Methods, 11 (2019) 36-43. doi: 10.1039/C8AY01998C
[33] L. Li, S. Tang, C. Wang, X. Lu, M. Jiang, H. Wu, X. Zhao, High gas storage capacities and stepwise adsorption in a UiO type metal–organic framework incorporating Lewis basic bipyridyl sites, Chemical Communications, 50 (2014) 2304-2307. doi: 10.1039/C3CC48275H
[34] A. Watson, Structure, chemistry and origins of gypsum crusts in southern Tunisia and the central Namib Desert, Sedimentology, 32 (1985) 855-875. doi: 10.1111/j.1365-3091.1985.tb00737.x
[35] H. Chen, C. P. Grey, Molten salt synthesis and high rate performance of the "desert-rose" form of $LiCoO_2$, Advanced Materials, 20 (2008) 2206-2210. doi: 10.1002/adma.200702655
[36] S. Niyogi, E. Bekyarova, M. E. Itkis, H. Zhang, K. Shepperd, J. Hicks, M. Sprinkle, C. Berger, C. N. Lau, W. A. Deheer, E. H. Conrad, R. C. Haddon, Spectroscopy of covalently functionalized graphene. Nano Letters, 10 (2010) 4061-4066. doi: 10.1021/nl1021128
[37] A. C. Ferrari, D. M. Basko, Raman spectroscopy as a versatile tool for studying the properties of graphene, Nature Nanotechnology, 8 (2013) 235-246. doi: 10.1038/nnano.2013.46
[38] T. H. Phan, H. Van Gorp, Z. Li, T. M. T. Huynh, Y. Fujita, L. Verstraete, S. Eyley, W. Thielemans, H. Uji-i, B. E. Hirsch, S. F. L. Mertens, J. Greenwood, O. Ivasenko, S. De Feyter, Graphite and graphene fairy circles: a bottom-up approach for the formation of nanocorrals, ACS Nano, 13 (2019) 5559−5571. doi: 10.1021/acsnano.9b00439
[39] https://www.ba.ic.cnr.it/softwareic/expo/
[40] S. F. L. Mertens, C. Xhoffer, B. C. De Cooman, E. Temmerman, Short-term deterioration of polymer-coated 55%Al-Zn – Part 1: Behavior of thin polymer films, Corrosion, 53 (1997) 381–388. doi: 10.5006/1.3280481

[41] S. F. L. Mertens, C. Xhoffer, B. C. De Cooman, E. Temmerman, Short-term deterioration of polymer-coated 55%Al-Zn – Part 2: Impedance model for inhibitor-modified surface, Corrosion, 55 (1999) 151-156. doi:10.5006/1.3283975; Corrosion 55 (1999) 631 (erratum)
[42] G. Hai, X. Jia, K. Zhang, X. Liu, Z. Wu, G. Wang, High-performance oxygen evolution catalyst using two-dimensional ultrathin metal-organic frameworks nanosheets, Nano Energy, 44 (2018) 345-352. doi: 10.1016/j.nanoen.2017.11.071

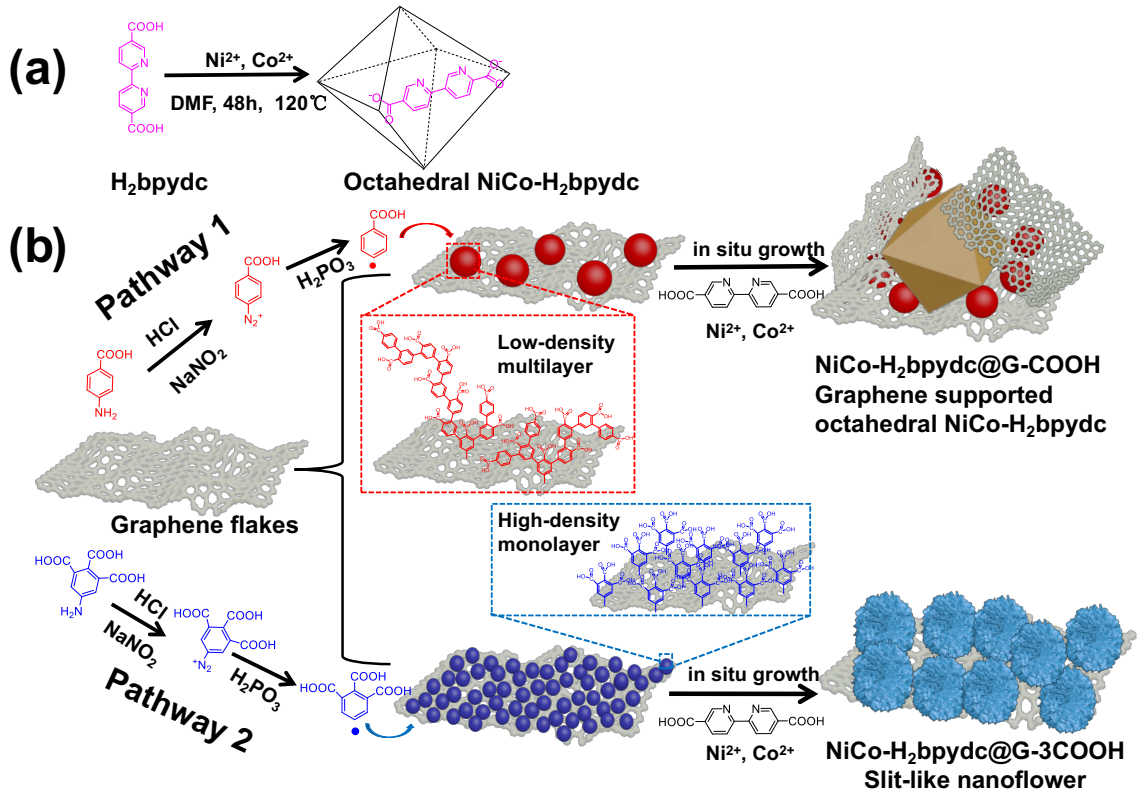

Figure 1. (a) Synthesis procedure of NiCo-H_2bpydc using solvothermal method. (b) Synthesis procedure of NiCo-H_2bpydc@G-COOH and NiCo-H_2bpydc@G-3COOH using different graphene templates with two covalent functionalization pathways.

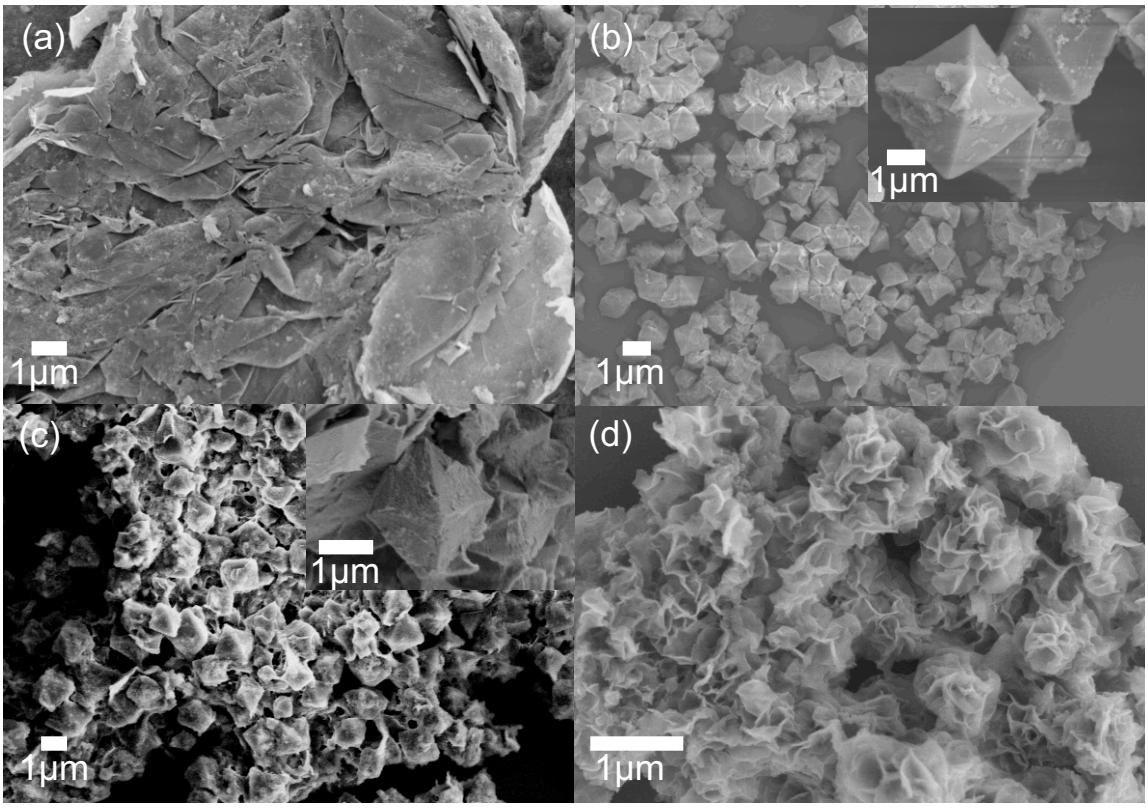

Figure 2. Morphology characterisation using scanning electron microscopy (SEM) of (a) pristine graphene flakes, (b) as-prepared NiCo-H_2bpydc (inset: high-resolution image), (c) NiCo-H_2bpydc@G-COOH (inset: co-existence of octahedral MOFs and graphene flakes), and (d) NiCo-H_2bpydc@G-3COOH with "desert rose" appearance.

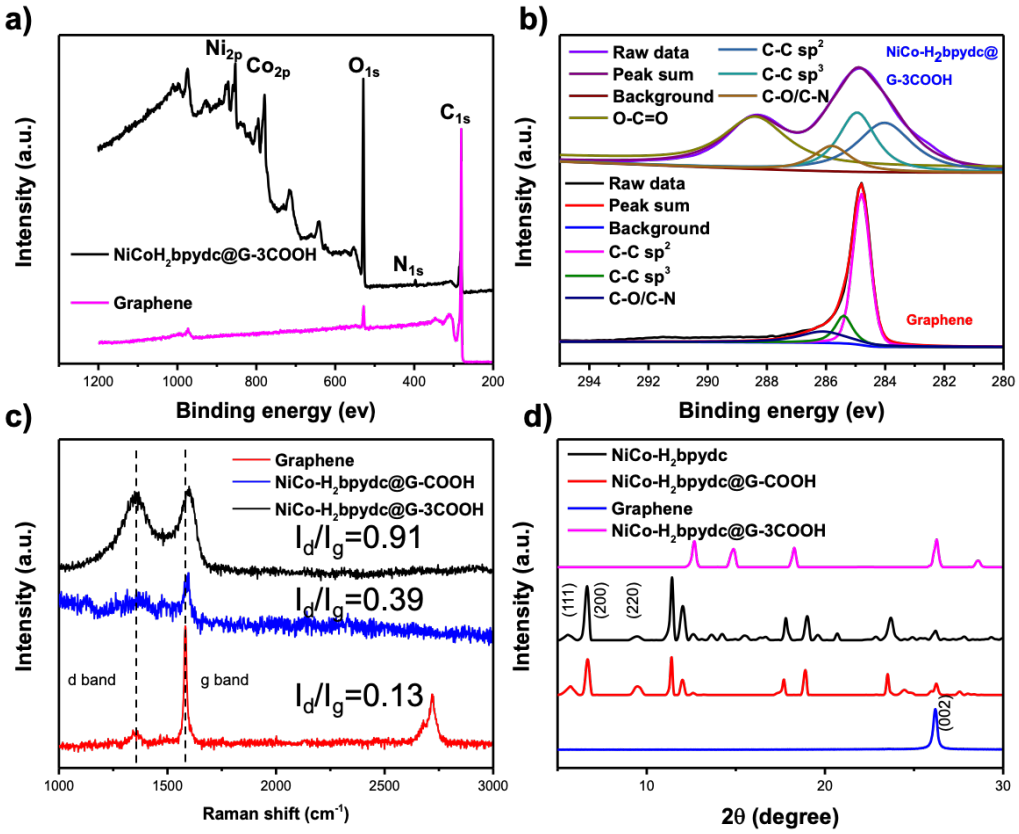

Figure 3. Structural and compositional characterisation of pristine graphene, NiCo-H_2bpydc and functionalized graphene supported NiCo-H_2bpydc. (a) XPS survey spectra; (b) High-resolution C_{1s} XPS scans; (c) Raman spectra with intensity ratios between d and g bands as indicated; (d) XRD patterns with tentative lattice indexation.

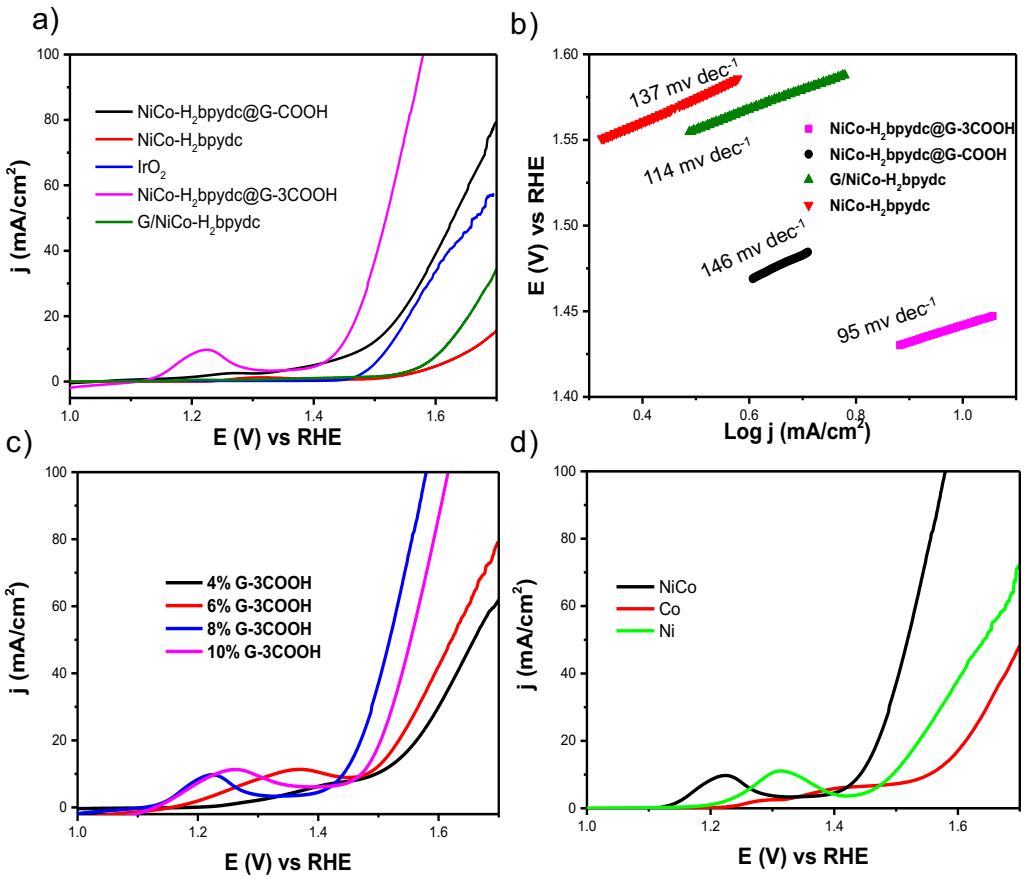

Figure 4. OER performance in 1M KOH. (a, c, d) linear sweep voltammetry and (b) Tafel plots generated from these. (c) Effect of G-3COOH/NiCo-H_2bpydc mass ratio, indicating an optimum (i.e. minimal overpotential) at 8 mass%. (d) Synergistic effect of combining Ni and Co metals, compared to Ni-H_2bpydc@G-3COOH and Co-H_2bpydc@G-3COOH

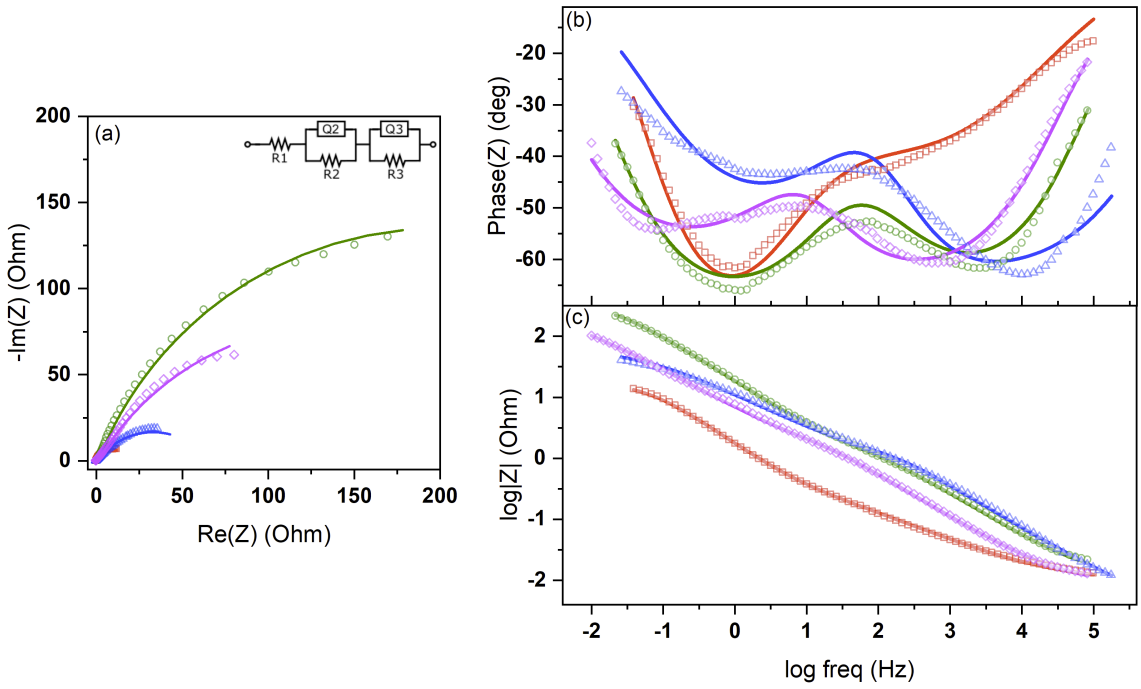

Figure 5. Electrochemical impedance measurements. (a) Nyquist and (b,c) Bode plots for graphene (red squares), NiCo-H_2bpydc@G-3COOH (blue triangles), NiCo-H_2bpydc@G-COOH (magenta diamonds), NiCo-H_2bpydc (green circles) on glassy carbon in 1M KOH at open circuit potential. Markers: data; continuous line: fit using the equivalent circuit shown as inset.

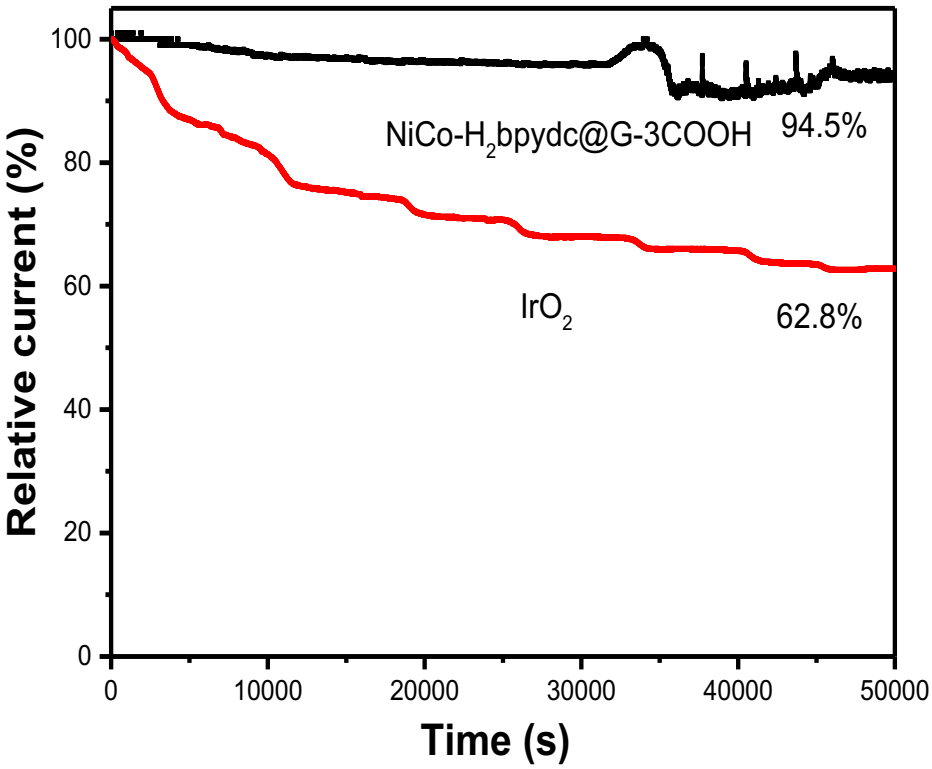

Figure 6. Long term stability test for NiCo-H2bpydc@G-3COOH and commercial IrO_2. Chronoamperometry in 1M KOH, 800 rpm, working electrode held at an overpotential of 250 mV.